Received 00th June 2016,
Accepted 00th June 2016

DOI: 10.1039/x0xx00000x

www.rsc.org/

Conformal oxide nanocoatings on electrodeposited 3D porous Ni films by atomic layer deposition

J. Zhang,[a] M. Coll,[b]* T. Puig,[b] E. Pellicer[a]* and J. Sort[c]*

A versatile chemical synthesis procedure to obtain Al_2O_3 and Co_2FeO_4 nanolayers conformally coating a three-dimensional (3D) porous Ni film is presented. First, porous Ni is grown by hydrogen bubble template-assisted electrodeposition. Subsequently, Al_2O_3 and Co_2FeO_4 layers, with thickness ranging from 5 nm to 25 nm, are directly deposited onto the pore walls by atomic layer deposition, while maintaining the porous architecture and magnetic properties of the Ni scaffold. The crystal structure, thickness and distribution of elements within the composite coatings are investigated in detail. The resulting magnetic and wettability properties are assessed. Contact angle tests reveal that 3D porous Ni films become more hydrophilic after coating with Al_2O_3 or Co_2FeO_4. From a technological point of view, the obtained composite porous films could be appealing for applications like magnetically-actuated micro/nano-electromechanical systems (MEMS/NEMS) or bio-MEMS/NEMS, among others.

1. Introduction

During the last decades, much progress has been made towards the development of novel synthetic approaches to prepare nanocomposite materials with tunable composition and microstructure. Multiphase composite materials are interesting since they combine the properties of the different constituents, often in a synergetic manner. The generation of large amounts of interfaces (as it is the case in nanocomposites) allows exploring novel interfacial coupling effects. In turn, porous structures, with much larger surface area–to–ratio compared to their fully dense counterparts, are very appealing to enhance certain physico-chemical properties. In terms of applications, nanostructured porous materials have received considerable attention since they hold great promise in areas like drug delivery systems,[1,2] batteries,[3] electrocatalysis,[4-6] supercapacitors[7] or magnetic micro/nano-electromechanical systems (MEMS/NEMS).[8] Recently, coating porous surfaces with different organic and inorganic materials has become an important route to obtain functionalized multiphase nanocomposites.[9,10] Depositing an insulating layer can reduce electrical shorting in MEMS/NEMS, while bio-MEMS/NEMS can benefit from the coating with a hydrophilic layer, which allows greater wetting with aqueous biological fluids.[11] In turn, coating porous materials with a biocompatible layer makes them more amenable to be used *in vivo*, such as for drug delivery or diagnosis.[12] Moreover, besides its protective role, a coating can also serve as an integrated functional unit. For example, 3D porous Ni films can function as scaffolds to anchor $Co(OH)_2$[13] or Si[14] to produce nanoporous composites with superior supercapacitor performance. A magnetic porous film can also host second phases that could provide electrical insulation, biocompatible surfaces, hydrophilic/hydrophobic properties or even enhanced magnetic performance.

In general, the synthesis of porous nanocomposite films is accomplished by chemical or electro-chemical reactions that occur at surface level. Nanocasting procedures using suitable precursors allow the filling of parent templates with oxide second phase materials of interest.[15] Nanoporous ceramic or polymeric templates (e.g., alumina or polycarbonate) can be filled with certain metals and alloys by electrodeposition.[16] Contrary to these examples, the complete or partial filling or coating of metallic porous templates with oxide materials is more challenging. The preparation procedures usually involve some heating steps, which can easily deteriorate the properties of the porous metallic framework, from both morphological (collapse of the pore structure) and compositional (oxidation) points of view. This is certainly deleterious for the subsequent implementation of these materials into real devices. Thus, the choice of an appropriate

[a] *Departament de Física, Universitat Autònoma de Barcelona, E-08193 Bellaterra, Barcelona, Catalonia, Spain. Email: eva.pellicer@uab.cat*
[b] *Institut de Ciència de Materials de Barcelona (ICMAB-CSIC), Campus UAB, E-08193, Bellaterra, Catalonia, Spain. Email: mcoll@icmab.es*
[c] *Institució Catalana de Recerca i Estudis Avançats (ICREA), E-08010 and Departament de Física, Universitat Autònoma de Barcelona, E-08193, Catalonia, Spain. Email: Jordi.sort@uab.cat*

Electronic Supplementary Information (ESI) available: [X-ray diffraction patterns of the investigated samples are provided as ESI]. See DOI: 10.1039/x0xx00000x

technique to grow this type of composites is of paramount importance. Very recently, we have demonstrated that porous CuNi supported ZnO hybrid films can be successfully prepared at relatively low temperature by combining electrodeposition with sol-gel drop casting in which (i) the matrix (or host) and the coating can be chosen independently, and (ii) the ferromagnetic properties of CuNi are preserved.[17] However, sol-gel deposition methods and some physical vapor deposition techniques are not so convenient to obtain a fully-continuous conformal coating of the parent template. Actually, atomic layer deposition (ALD) is the most suitable deposition technique to conformally coat materials exhibiting gaps, cavities, pores, trenches, out-of-sight surface and high-aspect ratio structures. This technique is based on alternate surface-limited reactions from the gaseous reactant to produce dense thin films and overlayers with nanoscale control, independently of the substrate's geometric complexity.[18,19] Therefore, it is a powerful technique that allows precise control over the composition and physical properties of nanoscaled materials and novel nanostructures.[20] To date, ALD of magnetic nanotubes and nanowires inside anodized alumina templates has been reported.[21,22,23] Interestingly, Al_2O_3 ALD films were successfully grown on a variety of magnetic substrates, including Co, Ni, NiFe and NiMn.[24] The aforementioned studies have proved the potential of ALD to deposit a wide variety of materials into narrow and high-aspect ratio pores.

In this work, we propose the combination of electrodeposition and ALD to obtain Ni/Al_2O_3, and Ni/Co_2FeO_4 magnetic nanocomposite porous films. 3D porous Ni films are prepared by one-step hydrogen bubble assisted galvanostatic electrodeposition,[25-27] while ALD is used to conformally coat the pores of the Ni scaffold with Al_2O_3 and Co_2FeO_4 nanolayers. Recent developments in the use of hydrogen bubble-templated method have led to the production of several magnetic porous films including Ni,[13,14] CuNi[28,29] or phase-separated Cu-Ni.[6] These films typically show macropores and, depending on the synthetic conditions, nanoporous dendritic walls, hence exhibiting a hierarchical porosity. Both macro- and nanopores could in principle host materials grown by ALD. In this study, Al_2O_3 and Co ferrite were chosen to coat the Ni skeleton. Al_2O_3 has a high dielectric constant (of about 7-10[30]); meanwhile, Co_2FeO_4 is ferrimagnetic. For the latter, conformal coating could result in strong magnetic exchange coupling between the ferromagnetic metallic porous matrix and the guest metal oxide component. Remarkably, the porous structure of the Ni matrices is maintained after the ALD process, which demonstrates that ALD permits the deposition of different types of oxide nanocoatings at relatively low, non-damaging temperatures. Structural and magnetic characterization reveals that Ni is not severely oxidized during the process. In addition, the resulting nanocomposite may become either more hydrophilic or hydrophobic than the parent Ni film, depending on the applied nanocoating. The proposed synthetic protocol could be readily extended to fabricate other 3D porous metal supported composite nanostructures for a variety of technological applications.

2. Experimental section

2.1 Preparation of the 3D porous Ni film

All solvents and chemicals were of analytical grade and used without further purification. Deposition of 3D porous Ni film was carried out in a double-jacketed single-compartment cell with an electrolyte containing 2 M NH_4Cl and 0.1 M $NiCl_2$ at a pH value of 3.5. The working electrode (WE) was Si/Ti(25 nm)/Au(125 nm) with an active area of 0.25 cm^2 (Ti and Au were grown by evaporation). Prior to deposition, the WE was cleaned with acetone, followed by diluted sulphuric acid and finally rinsed in water. A platinum wire served as the counter electrode and a dual-junction Ag|AgCl 3M KCl (E = + 0.210 V versus standard hydrogen electrode) was used as the reference electrode. The electrolyte was bubbled with nitrogen to deaerate the solution before electrodeposition. Electrodeposition was performed galvanostatically at j = -1 A cm^{-2} for 150 s with a gentle stirring speed of 300 rpm at room temperature. A cathodic polarization curve was recorded in order to identify the limiting current density regime. The resulting porous Ni films were washed with Milli-Q water and dried in air. The cathodic current efficiency was estimated to be ca. 76% on the basis of the pH drop after each deposition step.

Sample	A1	A2	A3	CFO/Ni
T	70℃	200℃	200℃	250℃
O source	H_2O	O_3	O_3	O_3
Precursor	TMA	TMA	TMA	$Co(Cp)_2$, $Fe(Cp)_2$
ALD mode	Pulse 0.3 s Expos 30 s	Pulse 0.3 s Expos 30 s	Pulse 0.7 s Expos 90 s	Fe: pulse 2s expos 30 s Co: pulse 1s expos 30 s

Table 1. ALD parameters used in this work. A1, A2 and A3 refer to Al_2O_3 coatings grown in porous Ni at the indicated experimental conditions. CFO/Ni stands for Co_2FeO_4 coating onto Ni. "Expos" represents the exposure time.

2.2 Fabrication of Ni supported Al_2O_3/Co_2FeO_4

ALD nanolayers onto the previously grown porous Ni films were prepared in a Cambridge Nanotech Savannah 100 reactor in exposure mode. Al_2O_3 coating was produced by alternate pulsing of trimethylaluminum (TMA) and ozone (O_3) at a deposition temperature of 70-200℃. For Co_2FeO_4 films, deposition was performed by alternate pulsing of cobaltocene ($Co(Cp)_2$), ferrocene ($Fe(Cp)_2$) and O_3 at 250℃.[31] Pulse and purge times were optimized for each material, as described in Table 1. Note that due to the well-known lower reactivity of

Fe(II) as a d^6 ion respect to Co(II) with d^7 electronic configuration,[32] the pulse length of $Fe(Cp)_2$ is longer than $Co(Cp)_2$ being both heated at 90°C. In this case, precursor pule ratio is $1Co(Cp)_2$:$2Fe(Cp)_2$.

2.3 Characterization of the structure and physical properties

Scanning electron microscopy (SEM) images and energy-dispersive X-ray spectroscopy (EDX) analyses were acquired using a Zeiss Merlin microscope operated at 3 kV and 15 kV, respectively. Transmission electron microscopy (TEM) and STEM-EDX analyses were performed on a Tecnai F20 HRTEM /STEM microscope operated at 200 kV. Cross sectional specimens were prepared by embedding the composites in EPON™ epoxy resin. Subsequently, a very thin slide was cut using a microtome apparatus and placed onto a carbon-coated Cu TEM grid.

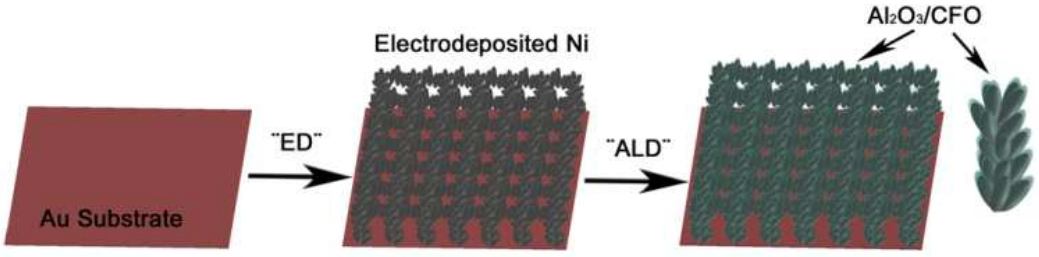

Fig. 1 Schematic picture illustrating the fabrication of 3D porous Ni supported Al_2O_3/ Co_2FeO_4 nanolayers. CFO denotes Co_2FeO_4.

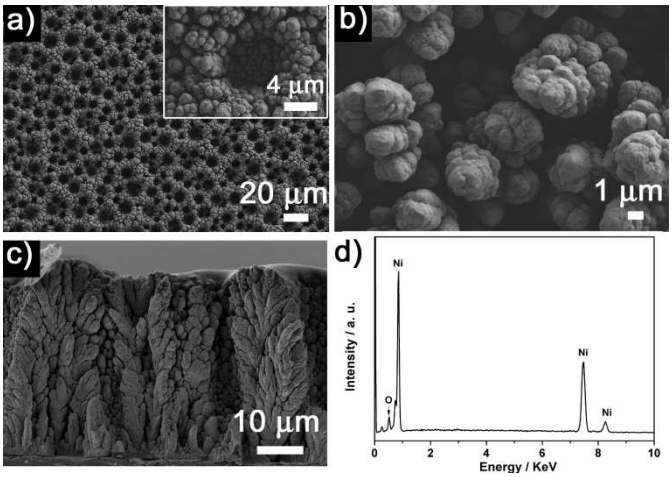

Fig. 2 SEM images of the 3D porous Ni film: a) on-top general view of the material (inset shows a detail of a macropore); b) on-top zoomed detail of the pore wall; c) cross-sectional view of the Ni film; d) EDX spectrum of the Ni film.

X-ray diffraction (XRD) patterns of the different samples were recorded on a Philips X'Pert diffractometer with a pixel[1D] detector in the 25-58° 2θ range (step size = 0.026°, total time = 1200 s) using Cu K_α radiation (λ = 0.154178 nm). Hysteresis loops were recorded at room temperature using a vibrating sample magnetometer (VSM) from Micro Sense, with a maximum applied magnetic field of 0.4 Tesla. Wettability properties of both uncoated and ALD-coated Ni samples were measured on a surface analyzer (Smartdrop, Femtofab) (sessile drop technique) at room temperature. 7 µL droplets of 5 wt% NaCl aqueous solution were deposited dropwise on the materials' surface using a microdispenser and the contact angle was determined.

3. Results and discussion

Fig. 1 schematically shows the preparation process followed to obtain the porous composite films. First, a hierarchically porous Ni film is electrodeposited onto the Au surface at a sufficiently negative current density. Ni possesses a high overpotential toward hydrogen evolution during electrodeposition in acidic media.[33] The generated hydrogen bubbles are absorbed onto the WE and then are liberated from the freshly grown Ni deposit to the electrolyte-air interface, acting as a dynamic template during the deposition. Hence, metal electrodeposition occurs between the hydrogen bubbles, yielding a film with a 3D porous architecture. The porous Ni film acts as a backbone to deposit Al_2O_3 and Co_2FeO_4 by ALD.

Shown in Fig. 2 are some representative SEM images of the as-deposited 3D porous Ni film. At low magnification (Fig. 2a), pores with an on-top circular shape are seen all over the surface, whose sizes range from 5 µm to 15 µm. Higher magnification observations (Fig. 2b) reveal that the pore walls consist of numerous tiny, interwoven, little protruding dendrites. The cross-sectional view of the deposits (Fig. 2c) confirms the ramified nature of the pore walls. The deposited Ni thickness is approximately 40 µm. Interestingly, the macropores extend from the outermost surface almost down to the substrate, having a depth of ~30 µm. This demonstrates the rather high aspect-ratio of the pores. A representative EDX spectrum of the Ni film is shown in Fig. 2d. Ni element together with a very low oxygen signal are detected, which proves that the porous layer is almost entirely metallic.

To obtain a smooth coating that perfectly replicates the template surface it is important to identify the deposition conditions to be within the ALD window. This window is a

temperature region where the growth rate is constant and assures a tight control of the process and high reproducibility. Working outside this window means that undesired processes can occur, including decomposition or desorption of the precursor (temperature too high), precursor condensation or insufficient reactivity (temperature too low). As a result, the growth rate is modified and the level of impurities in the film can increase. For Al_2O_3, which is the most widely studied material in ALD because it has a behavior close to ideal (i.e., the ALD window is well established), the following reaction mechanism has been proposed:[34] (1) diffusion of the aluminum precursor ($Al(CH_3)_3$) into the near surface region of the host material, (2) reaction and saturation of the substrate surface with Al-CH_3 species and purge to eliminate reaction products and excess of the precursor (3) diffusion of the oxygen precursor into the Al-CH_3 surface, (4) reaction and saturation of the surface with Al-OH species followed by a purge to eliminate the reaction products.

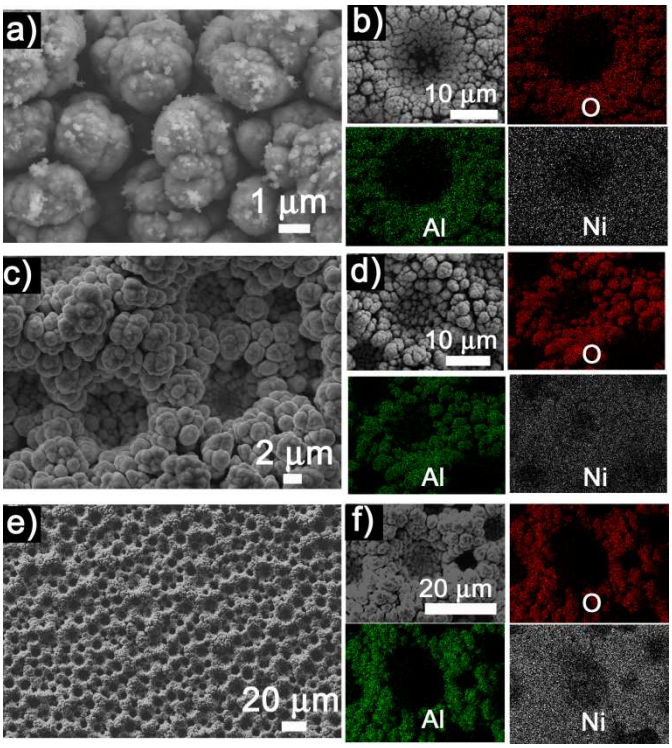

Fig. 3 On-top SEM images of a) A1, c) A2 and e) A3 nanocomposites. EDX mapping distribution of Al, O, and Ni elements in b) A1, d) A2 and f) A3 composites, obtained from the zoomed SEM images shown on the left.

This is defined as the first ALD cycle and it is repeated as many times as required to obtain the desired thickness. This process allows the formation of a dense Al_2O_3 film that coats the host material. According to the literature, the growth of a continuous thin layer of Al_2O_3 by ALD is possible at a temperature as low as 33°C[35] but the reaction kinetics is slow in this case (since the reaction is thermally activated) and hence higher temperatures are sometimes required.[36] The completion of the reaction, *i.e.* full coalescence of the Al_2O_3 clusters, needs longer time at lower temperatures.

It should be noted that such an ideal behavior is in many materials not easy to achieve. For high aspect ratio structures, exposure mode (i.e. the precursor is left longer time in the reaction time) are routinely used in order to ensure conformal coating. Here, as detailed in Table 1, several experiments have been performed varying the deposition temperature, oxygen source, precursor pulse and exposure time, to identify the optimal ALD conditions for both Al_2O_3 and Co_2FeO_4.

SEM images and the corresponding EDX mappings for A1, A2 and A3 composites are shown in Fig. 3. Fig. 3a reveals that the surface of A1 composite is rather rough, featuring small clusters instead of a continuous shell. Nevertheless, Al, O and Ni elements were homogeneously distributed in the corresponding EDX mapping image (Fig. 3b) (note that shadowing effects during EDX analysis preclude detection of elements inside the pores). Thus, from the morphology observed in Fig. 3a it is suggested that these deposition conditions are not optimal. It is likely that the reaction temperature is too low (precursor condensation-insufficient reactivity).

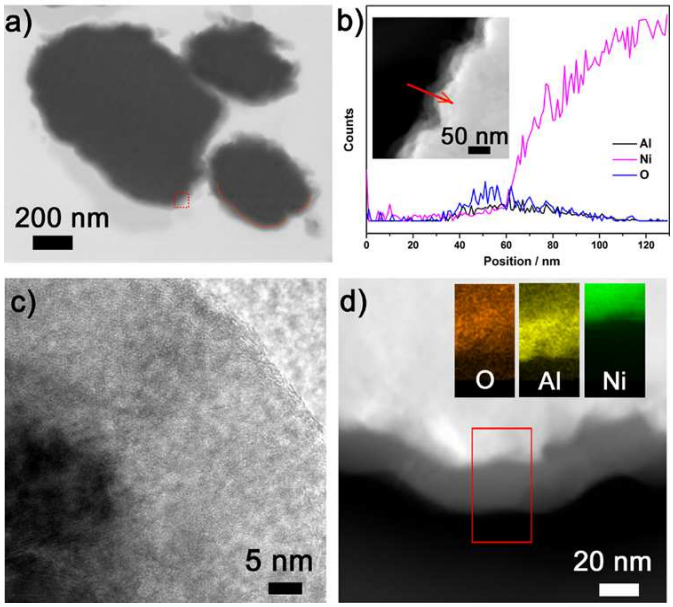

Fig. 4 a) SEM image of A3 nanocomposite slice; b) line-scan STEM-EDX analysis across the interface between Ni and Al_2O_3, as indicated by the red arrow in the insert STEM image; c) HRTEM image of the area enclosed with the red dotted square in a); d) EDX elemental distribution of O, Al and Ni in the interfacial area enclosed within the red rectangle.

When the temperature is increased to 200°C and, simultaneously, water is replaced by ozone (more reactive oxygen source), the Ni surface becomes smoother. An Al_2O_3 layer coating the Ni grains is apparently visible from Fig. 3c and 3e. Remarkably, the porosity of the Ni matrix is preserved after the Al_2O_3 deposition, indicating that the oxide nanolayer is extremely conformal to the Ni skeleton. EDX elemental distribution images of A2 and A3 composites (Fig. 3d, f) show that Al and O are distributed in a parallel way, which indicate that the relative Al_2O_3 coverage is completely uniform for reactant exposure times of 30 s. This finding is similar to that

reported by George *et al*.[20] who also demonstrated that a reactant exposure of 30 s was sufficient to obtain a nearly conformal coating in high aspect-ratio structures.

To further assess the conformal coating of Ni with Al_2O_3, sample A3 was embedded in resin and sliced in order to gain insight into Ni/Al_2O_3 interface. Sample preparation was very challenging since the material was prone to break into several pieces during the slicing owing to their 3D porous structure. Nevertheless, reasonably large isolated fragments of the material could be found by SEM, as shown in Fig. 4a. These fragments, featuring a dark contrast, are surrounded by a brighter-contrast shell, as indicated with the solid orange line in Fig. 4a. Note that during the preparation of composite slices for TEM observations, not only regions close to the film surface were analyzed but also slices close the Au surface. In all cases, the ALD layer was found to conformally coat the Ni film.

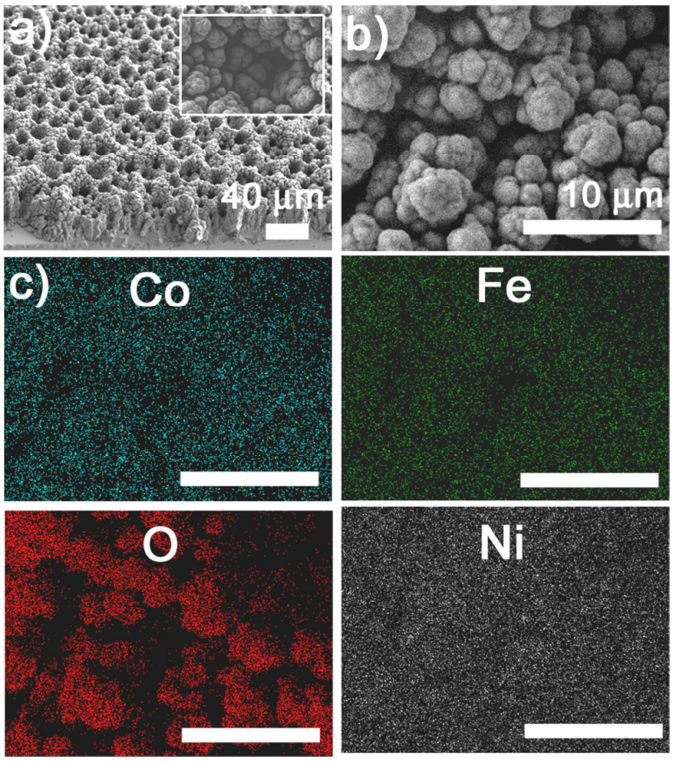

Fig. 5 a) Oblique-sectional (insert, magnified) view of 3D porous Ni-supported cobalt ferrite, b) magnified SEM image; c) corresponding Co, Fe, O and Ni EDX mappings.

STEM-EDX line scan analysis was performed in order to determine the composition profile across the interface (Fig. 4b). An EDX line scan was done along the red arrow depicted in the inset STEM image of Fig. 4b, which embraces a translucent thin layer and a denser bright region. As the electron beam is scanned towards the Ni matrix, Al and O signals first appear at 35 nm from the initial scanning point and vanish at approximately 100 nm. Conversely, the Ni signal monotonically increases from around 60 nm, which indicates that the Al_2O_3 coating has a thickness of about 25 nm. Remarkably, there is no abrupt switching from Al and O signals to Ni signal but, instead, they coexist within a few nanometers interval. This suggests the formation of a mixed Al/Ni oxide at the interface. This was further proved by STEM-EDX elemental distribution mapping (Fig. 4d), *i.e.*, Ni-oxide or some mixed $(Al,Ni)_xO_y$ phases may exist at the interface region. Hence, the structure of the interface can be defined as $Al_2O_3/(Al,Ni)_xO_y$/Ni. Fig. 4c actually corresponds to the HRTEM of the region enclosed in the small red box in Fig. 4a. It is likely that the as-deposited Al_2O_3 layer is amorphous since lattice fringes were not detected. The amorphous nature of Al_2O_3 was further confirmed by θ-2θ scan X-ray diffraction (XRD) (Fig. S1). For comparison, the XRD data of uncoated Ni is shown. Besides a peak coming from the Au surface, the diffraction peaks corresponding to Ni (111) and Ni (200) reflections of face-centered cubic (*fcc*) structure (PCPDF 04-0850) remain virtually unchanged after ALD coating of Ni scaffold with Al_2O_3. Hence, the 3D porous Ni withstands the ALD process both morphologically and crystallographically to a great extent.

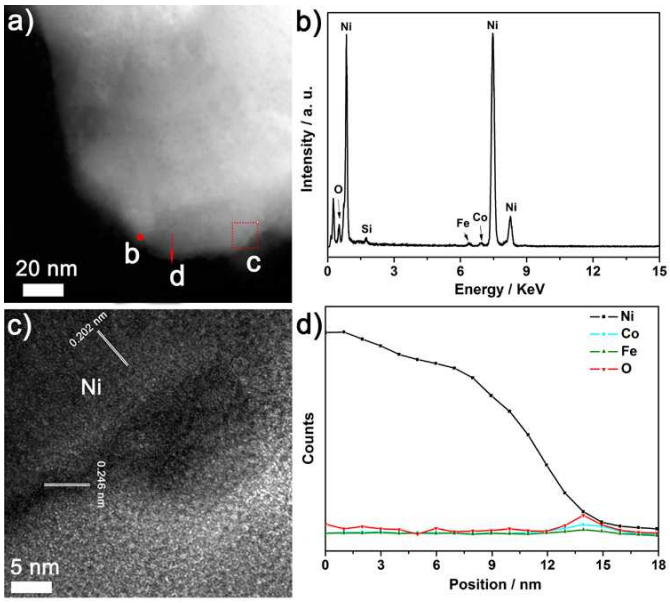

Fig. 6 a) TEM image of the cross sectional view of Ni/Co_2FeO_4 sample; b) EDX spectrum corresponding to the red dot "b" in a); c) HRTEM image of the area enclosed with the red square labeled as "c" in panel a); d) line-scan STEM-EDX analysis across the edge depicted with the red arrow "d" in panel a).

The typical peaks of crystalline Al_2O_3 in the range 25°-55° are not observed in the XRD pattern. Instead, two peaks at 33° and 37° were detected, which can be attributed to a Ni_xO_y phase. This result further confirms the hypothesis that the Ni outermost surface was slightly oxidized during ALD (i.e., the interface can be described as $Al_2O_3/(Al,Ni)_xO_y$/Ni).

Based on these findings, 3D porous Ni supported cobalt ferrite composite films (Co_2FeO_4) were prepared using a similar protocol (Table 1). Metallocenes are ideal precursors for ALD owing to their thermo stability, high volatility and reactivity toward oxidation to a certain degree.[37] Fig. 5 depicts typical SEM images of the as-prepared 3D porous Ni-supported cobalt ferrite. As for Al_2O_3 coating, the porous morphology provided by the Ni matrix remains unchanged (Fig. 5a,b) and Co, Fe and O elements are evenly distributed (Fig. 5c). A Ni/Co_2FeO_4 specimen for cross sectional view was also prepared to assess

the quality of the oxide nanocoating. As displayed in the TEM image (Fig. 6a), the sliced porous film shows a nanosheet morphology, being the interface between the metal and the oxide layer less defined compared to Al_2O_3 case. For this reason, a more detailed characterization was carried out near the edge. When the electron beam was spotted onto the red dot "b" in Fig. 6a, Ni, Fe, Co and O signals appeared in the EDX spectrum (Fig. 6b). The relative proportion between Co, Fe and O yielded a composition close to Co_2FeO_4, as expected. When the electron beam was swept from the body to the edge (red arrow in Fig. 6a), the Ni signal gradually decreases down to negligible levels (Fig. 6d). Meanwhile, Co, Fe and O signals simultaneously increase at the particle edge until a maximum value, leading to a Co/Fe/O atomic ratio of 2:1:4, in agreement with previous studies of ALD Co_2FeO_4 thin films.[32] The interface from pure Ni to Co_2FeO_4 is not well defined (as it was also the case for Ni/Al_2O_3), but rather a transition layer is formed which embraces the four elements. The thickness of this transition layer is around 5 nm. Fig. 6c shows a HRTEM image of the area enclosed in the red box in Fig. 6a. The porous Ni template is slightly brighter than the Co_2FeO_4 nanocoating, which is about 5 nm thick. Both Ni and Co_2FeO_4 are polycrystalline with clear lattic fringes. The interplanar distance of d = 0.202 nm can be assigned to the (111) *fcc* phase of Ni, whereas d = 0.246 nm matches the (311) *fcc* of Co_2FeO_4. The formation of crystalline cobalt ferrite is also confirmed by the XRD pattern shown in Fig. S2. Namely, the small peak at 36.02° after ALD can be ascribed to the (311) reflection of Co_2FeO_4.

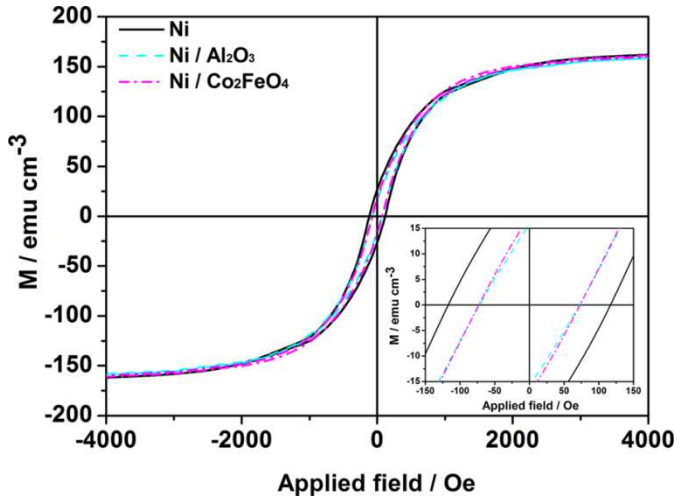

Fig. 7 Room temperature hysteresis loops of uncoated Ni, Ni/Al_2O_3 and Ni/Co_2FeO_4 composite porous films.

Room-temperature magnetic hysteresis loops of the uncoated Ni, Ni/Al_2O_3 and Ni/Co_2FeO_4 porous films are shown in Fig. 7. The saturation magnetization (M_s) for the Ni/Al_2O_3 nanocomposite films (159.1 emu cm^{-3}) is slightly lower than for pure Ni (162.0 emu cm^{-3}). This can be ascribed to the presence of a small amount of NiO (in agreement with the results from XRD and STEM-EDX), which is antiferromagnetic and hence exhibits virtually zero net magnetization. Note that the porosity degree is not taken into account in the magnetization (M) normalization; that is, the volume is calculated from the real "geometrical" thickness. When comparing the experimental and tabulated M_s value for pure Ni (491 emu cm^{-3}), it comes out that the porosity degree of the Ni layer is approximately 67 vol%. Although NiO is antiferromagnetic, no exchange bias effects (e.g., loop shift[38] or enhanced coercivity[39]) are observed, mainly because the relative amount of NiO is very low compared to that of Ni and exchange bias effects are known to be inversely proportional to the thickness of the ferromagnetic counterpart.[38] Similarly, because of the relatively low volume fraction of Co_2FeO_4, its contribution to the overall hysteresis loop of the Ni/Co_2FeO_4 film is also very small.

The hysteresis loops also reveal that the H_c values of the composite films (around 73 Oe) are smaller compared to H_c of uncoated Ni (118 Oe). This decrease of coercivity is probably related to thermally-induced microstructural changes that occur in metallic Ni during the ALD process. Actually, Fig. S1 and S2 reveal that the width of the XRD peaks of Ni becomes narrower after ALD (particularly for Ni/Co_2FeO_4), which indicates that the crystallite size of Ni increases. The average crystallite size for Ni, estimated from XRD Rietveld refinements, increases from approximately 35 nm (for uncoated Ni) to 45 nm in the case of Ni/Al_2O_3 and 60 nm for Ni/ Co_2FeO_4 composites. In general, grain boundaries hinder and pin the propagation of magnetic domain walls. Hence, H_c, in polycrystalline magnetic alloys, is inversely proportional to the grain size.[40] Also the release of microstrains associated with the ALD thermal treatments could contribute to reduce the coercivity.

The wettability of Ni, Ni/Al_2O_3 and Ni/Co_2FeO_4 films was characterized by the sessile drop technique, using 7 µL of 5 wt% NaCl droplets. Fig. 8 shows the shape of NaCl droplets deposited onto the three different surfaces. The contact angle attains the highest value at the surface of uncoated Ni (139°) (Fig. 8a). The contact angle values decrease to 119° and 102° for Ni/Al_2O_3 and Ni/Co_2FeO_4, respectively. Variations in surface roughness could account for the observed differences among the three samples. However, surface roughness is similar since both Al_2O_3 and Co_2FeO_4 coatings are really thin and conformal. In fact, variations of the contact angle in solids not only depend on surface roughness, but are also related to the surface energy of the investigated materials.[41] Metal oxides have lower surface energy than pure metals since the latter tend to react with the atoms (molecules) from the surrounding in an attempt to form a passive layer (e.g., metal oxide) with lower energy level. In general, most molecular liquids form lower contact angles on materials with a higher surface energy. However, this is opposite to what is observed here. Nonetheless, the wettability of a surface is also determined by the outermost chemical groups at the solid. Metal oxide surfaces are often fully or partly covered with OH groups which are usually formed by the interaction of water with the metal ions at the surface.[42] The surface-anchored hydroxyl groups participate in hydrogen bonding with the static aqueous droplets, thus increasing the wettability of the material. Thus, our results reveal that 3D porous Ni structures

coated with metal oxide nanolayers are slightly more hydrophilic than the parent Ni template.

In biological systems, relatively hydrophilic coatings allow the formation of tightly adherent layers of aqueous biological fluids with high lubricity to the material. Therefore, our oxide coatings would prevent from Ni ion leaching, which is a concern since Ni can pose cytotoxicity problems.

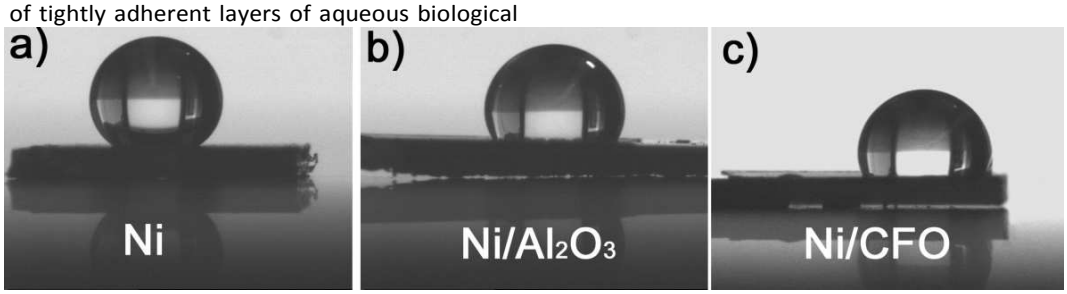

Fig. 8 Optical photographs of an aqueous sodium chloride droplet (7 μm) onto the surface of (a) Ni, (b) Ni/Al_2O_3 and (c) Ni/Co_2FeO_4 porous films.

This combination of metals and oxides in a single 3D porous structure could also be appealing as building blocks in MEMS/NEMS. The use of Al_2O_3 would possibly reduce the tendency toward electrical shorting[29] since Al_2O_3 has a high dielectric constant (in the range of 7-10) and an electrical resistance of about 1015 Ω·cm. Likewise, Ni/Co_2FeO_4 is a material with potential applications in spintronics and as spring-magnet layered composites. Moreover, gas sensor based on cobalt ferrite showed high response, good selectivity to low concentration of ethanol.[43] Yet the investigation on gas-sensing properties of cobalt ferrite is really limited, and further experimental proof is nevertheless still necessary. This indicates that the here-presented synthetic strategy of combining electrodeposition and ALD is very convenient to produce magnetic nanocomposite porous films with potential applications in a wide range of technological fields.

4. Conclusions

The possibility to combine electrodeposition with ALD to prepare 3D porous magnetic metals conformally coated with metal oxide nanolayers, namely Ni/Al_2O_3 and Ni/Co_2FeO_4, is demonstrated. Due to the nature of the presented approach the host (metal) and guest (metal oxide) materials can be chosen with certain degree of freedom. We demonstrate that both the hierarchical porosity and magnetic properties of the parent metallic Ni template are maintained after ALD step. Moreover, the presence of a nanometer-thick layer of Al_2O_3 or Co_2FeO_4 covering the Ni scaffold improves surface wettability. The procedure could be extended to prepare other magnetic compositions obtained using the same protocol. Owing to the synergies emerged between the host and the guest components, these nanocomposite magnetic porous films are promising candidates for widespread technology areas, such as biological applications, magnetic sensors or magnetic micro/nano-electromechanical systems (MEMS/NEMS), amongst others.

Acknowledgements

This work has been partially funded by the 2014-SGR-1015 and 2014-SGR-150 projects from the Generalitat de Catalunya, the MAT2014-57960-C3-1-R and MAT2014-51778-C2-1-R projects from the Spanish Ministerio de Economía y Competitividad (MINECO) and associated FEDER, and the SPIN-PORICS 2014-Consolidator Grant from the European Research Council (Grant Agreement 648454). J.Z. is grateful to the China Scholarship Council (CSC) for the PhD grant. E.P. and M.C. are grateful to MINECO for the "Ramon y Cajal" contract (RYC-2012-10839, RYC-2013-12448). ICMAB acknowledges support from the Severo Ochoa Program (MINECO, Grant No. SEV-2015-0496).

Notes and references

1 M. A. Shahbazi, B. Herranz, H. A. Santos, *Biomater.,* 2012, **2,** 1-17.
2 M. Mustapic, M. S. A. Hossain, J. Horvat, P. Wagner, D. R. G. Mitchell, J. H. Kim, G. Alici, Y. Nakayama, B. Martinac, *Micropor. Mesopor. Mat*., 2016, **226**, 243-250.
3 Q. Q. Xiong, J. P. Tu, Y. Lu, J. Chen, Y. X. Yu, X. L. Wang, C. D. Gu, *J. Mater. Chem*., 2012, **22**, 18639-18645.
4 F. Yang, K. Cheng, X. Xue, J. Yin, G. Wang, D. Cao, *Electrochim. Acta,* 2013, **107**, 194-199.
5 X. Qian, T. Hang, S. Shanmugam, M. Li, *ACS Appl. Mater. Interfaces,* 2015, **7**, 15716-15725.
6 J. Zhang, M. D. Baró, E. Pellicer, J. Sort, *Nanoscale,* 2014, **6**, 12490-12499.
7 G. Wang, H. Liu, J. Horvat, B. Wang, S. Qiao, J. Park, H. Ahn, *Chem. Eur. J*., 2010, **16**, 11020-11027.
8 E. Pellicer, S. Pané, V. Panagiotopoulou, S. Fusco, K. M. Sivaraman, S. Suriñach, M. D. Baró, B. J. Nelson, J. Sort, *Int. J. Electrochem. Sci*., 2012, **7**, 4014-4029.
9 W. Wang, M. Tian, A. Abdulagatov, S. M. George, Y. C. Lee, R. Yang, *Nano Lett.,* 2012, **12**, 655-660.
10 D. Li, Q. Zheng, Y. Wang, H. Chen, *Polym. Chem.,* 2014, **5**, 14-24.
11 V. S. Sundram, S. Nesappan, *Int. J. Nano Biomater.,* 2014, **5**, 243-262.
12 B. Sahoo, K. S. P. Devi, S. Dutta, T. K. Maiti, P. Pramanik, D. Dhara, *J. Colloid. Interf. Sci.,* 2014, **431**, 31-41.
13 X. H. Xia, J. P.Tu, Y. Q. Zhang, Y. J. Mai, X. L. Wang, C. D. Gu, X. B. Zhao, *J. Phys. Chem. C,* 2011, **115**, 22662-22668.
14 Y. Q. Zhang, X. H. Xia, X. L. Wang, Y. J. Mai, S. J. Shi, Y. Y. Tang, C. G. Gu, J. P. Tu, *J. Power Source,* 2012, **213**, 106-111.
15 E. Pellicer, M. Cabo, A. López-Ortega, M. Estrader, L. Yedra, S. Estradé, F. Peiró, Z. Saghi, P. Midgley, E. Rossinyol, I. V. Golosovsky, A. Mayoral, J. D. Prades, S. Suriñach, M. D. Baró, J. Sort, J. Nogués, *Nanoscale,* 2013, **5**, 5561-5567.

16 J. Zhang, S. Agramunt-Puig, N. Del-Valle, C. Navau, M. D. Baró, S. Estradé, F. Peiró, S. Pané, B. J. Nelson, A. Sánchez, J. Nogués, E. Pellicer, J. Sort, *ACS Appl. Mater. Interfaces*, 2016, **8**, 4109–4117.
17 M. Guerrero, J. Zhang, A. Altube, E. G. Lecina, M. Roldan, M. D. Baró, E. Pellicer, J. Sort, *Sci. Technol. Adv. Mater*., 2016, **17**, 177-187.
18 C. Bae, H. Shin, K. Nielsch, *MRS Bulletin,* 2011, **36**, 887-897.
19 R. W. Johnson, A. Hultqvist, S. F. Bent, *Mater. Today,* 2014, **17**, 236-246.
20 M. Knez, K. Nielsch, L. Niinistö, *Adv. Mater.,* 2007, **19**, 3425-3438.
21 J. W. Elam, D. Routkevitch, P. P. Mardilovich, S. M. George, *Chem. Mater*., 2003, **15**, 3507-3517.
22 M. Daub, M. Knez, U. Goesele, K. Nielsch, *J. Appl. Phys*., 2007, **101**, 09J111.
23 J. Bachmann, J. Jing, M. Knez, S. Barth, H. Shen, S. Mathur, U. Gösele, K. Nielsch, J. Am. Chem. Soc. 2007, 129, 9554-9555.
24 M. D. Groner, J. W. Elam, F. H. Fabreguette, S. M. George, *Thin Solid Films,* 2002, **413**, 186-197.
25 H. C. Shin, J. Dong, M. Liu, *Adv. Mater*., 2003, **15**, 1610-1614.
26 Y. Li, W. Z. Jia, Y. Y. Song, X. H. Xia, *Chem. Mater*., 2007, **19**, 5758-5764.
27 S. Cherevko, X. Xing, C. Chung, *Electrochem. Commun*., 2010, **12,** 467-470.
28 L. Mattarozzi, S. Cattarin, N. Comisso, R. Gerbasi, P. Guerriero, M. Musiani, L. V. Gómez, E. Verlato, *ESC Electrochem. Lett*., 2013, **2**, D58-D60.
29 S. Eugénio, T. M. Silva, M. J. Carmezim, R. G. Duarte, M. F. Montemor, *J. Appl. Electrochem*., 2014, **44**, 455-465.
30 S. M. George, C. F. Herrmann, *Al_2O_3 Atomic Layer Deposition to Enhance the Deposition of Hydrophilic Coating on Micro-Electromechanical Devices*. US 20050012975 A1, January 20, 2005.
31 M. Coll, J. M. Montero Moreno, J. Gázquez, K. Nielsch, X. Obradors, T. Puig, *Adv. Funct. Mater.,* 2014, **24**, 5368–5374.
32 R. H. Grabtree, *The Organometallic Chemistry of the Transition Metals,* 2nd ed.; Wiley: New York, 1994.
33 J. Lu, T. Xiong, W. Zhou, L. Yang, Z. Tang, S. Chen, *ACS Appl. Mater. Interfaces,* 2016, **8**, 5065-5069.
34 C. A. Wilson, R. K. Grubbs, S. M. George, *Chem. Mater*., 2005, **17**, 5625-5634.
35 M. D. Groner, F. H. Fabreguette, J. W. Elam, S. M. George, *Chem. Mater*., 2004, **16**, 639-645.
36 A. C. Dillon, A. W. Ott, J. D. Way, S. M. George, *Surf. Sci*., 1995, **322**, 230-242.
37 Y. T. Chong, E. M. Y. Yau, K. Nielsch, J. Bachmann, *Chem. Mater*. 2010, **22**, 6506-6508.
38 J. Nogués, I. K. Schuller, *J. Magn. Magn. Mater.,* 1999, **192**, 203–232.
39 J. Sort, S. Suriñach, J. S. Muñoz, M. D. Baró, J. Nogués, G. Chouteau, V. Skumryev, G. C. Hadjipanayis, *Phys. Rev. B,* 2002, **65**, 174420.
40 R. Ramesh, G. Thomas, B. M. Ma, *J. Appl. Phys.,* 1988, **64**, 6416-6423.
41 M. Ma, R. M. Hill, *Curr. Opin. Colloid Interface Sci*., 2006, **11**, 193-202.
42 D. Cappus, C. Xu, D. Ehrlich, B. Dillmann, C. A. Ventnce Jr., K. Al Shamery, H. Kuhlenbeck H.-J. Freund, *Chem. Phys.,* 1993, **177**, 533-546.
43 C Xiangfeng, J. Dongli, G. Yu, Z. Chenmou, *Sens. Actuators B,* 2006, **120**, 177-181.